Int J Adv Manuf Technol (2017) 89:885–895
DOI 10.1007/s00170-016-9135-x

ORIGINAL ARTICLE

Investigation on direct laser powder deposition of 18 Ni (300) marage steel using mathematical model and experimental characterisation

Sabina Luisa Campanelli[1] · **Andrea Angelastro**[1] · **Carmine Gabriele Signorile**[1] · **Giuseppe Casalino**[1]

Received: 22 March 2016 / Accepted: 4 July 2016 / Published online: 13 July 2016

Abstract Direct laser powder deposition (DLPD) is a laser process that can produce fully dense components from powders for production and repairing purposes. Marages are high-strength steels that are hardened through ageing treatment. This work presents a study which integrated the numerical and experimental approaches, for the evaluation of the properties of 18 Ni (300) laser deposited marage powder. The powder was deposited onto AISI 304 substrate by a CO_2 laser. During the experiments, laser power, scanning speed, powder flow rate and degree of overlapping varied according to a Taguchi plan. In particular, the degree of overlapping between adjacent layers and between successive tracks was calculated using an analytical model. Density, porosity, dilution, microstructure, adhesion to the substrate and microhardness of multilayer samples were evaluated using statistical algorithms. Both clad-substrate and clad-clad interfaces were characterised by metallographic and SEM analysis. High-density samples, with a satisfactory level of porosity, for successful additive and part repair applications, were fabricated through the method proposed and characterised in this paper.

Keywords Direct laser powder deposition · Marage steel · Mathematical model · Experimental characterisation

✉ Giuseppe Casalino
g.casalino@poliba.it

[1] Politecnico di Bari, Viale Japigia, 182, 70126 Bari, Italy

List of symbols

d	Spot diameter (mm)
D	Dilution
E_d	Energy density (J/mm^2)
H	Clad height (mm)
m_l	Lacquer mass (g)
$m_{l+s}^{H_2O}$	Mass of coated sample in water (g)
m_s	Sample mass (g)
$O_{\%}$	Overlapping ratio
P	Laser power (W)
Q	Powder flow rate (g/min)
R	Theoretical circumference radius (mm)
R_d	Relative density
Sx	Hatch spacing along x direction (mm)
Sz	Step height (mm)
v	Scanning speed (mm/min)
W	Clad width (mm)
ρ_s	Sample density (g/cm^3)
ρ_l	Lacquer density (g/cm^3)
ρ_{H_2O}	Water density (g/cm^3)

1 Introduction

ASTM International Committee F42 in ASTM F2792-12a (AM) defined additive manufacturing technology as "process of joining materials to make objects from 3D model data, usually layer-upon-layer, as opposed to subtractive manufacturing methodologies, such as traditional machining" [1].

Several additive processes belong to this group such as direct metal deposition (DMD), direct light fabrication

(DLF), laser engineered net shaping (LENS), Lasform (Aeromet), Lightspeed (Lockheed Martin), LaserCast (ARL Penn State), laser direct casting (LDC), laser powder fusion (LPF) and laser metal deposition (LMD). Direct laser powder deposition uses a laser beam and a metal powder. The laser beam melts the powder, which forms a deposit on a metallic substrate by fusion bonding. Direct laser powder deposition (DLPD) is well suited to several industrial applications since it is successful for repairing and rebuilding worn or damaged components, to manufacture new components and to apply wear- and corrosion-resistant coatings [2].

DLPD was born on principles of laser cladding because it focuses the laser beam energy onto a metal substrate so it melts both the irradiated surface and powder. By following a specific path onto each layer, the laser scanning can produce three-dimensional components. The design has a very great potentiality in the production of complex 3D shapes also with materials hard to work with conventional processes [3]. Lu et al. analysed the effect of process parameters, in order to realise a steam turbine blade using 316L powder [4]. Peng et al. studied a closed-loop control for this process in order to create a thin wall [5]. The five-axis systems allow building components that require the deposition of layers along different orientations. This result can be achieved either by tilting the laser beam and the nozzle, which supplies powder, or by tilting the piece under construction. Thus, the axis of the laser beam is always normal to the deposition plane. Differently from selection laser melting (SLS), DLPD produces protruding or overhanging parts without the need of support like a powder bed [6–8].

Different industrial fields like aeronautical and machining sectors show an increasing interest in this technique. Bi and Gasser studied the restoration of nickel-base turbine blade knife-edges, using a control of molten pool temperature capable to regulate the laser power [9]. Wilson et al. showed that the reparation of a 316L turbine blade with DLPD improved the carbon footprint and reduced the energy consumption with respect to the replacement with a new blade [10].

The reduction of porosity is one of the main goals that ensure good mechanical properties. During deposition process, both interlayer and intralayer pores can form.

Table 1 Chemical composition of the employed powder determined by EDX analysis

Powder Material	Ni	Mo	Co	Ti	C	Fe
18 Ni (300) steel	18.8	4.2	10.2	0.88	0.02	Balance

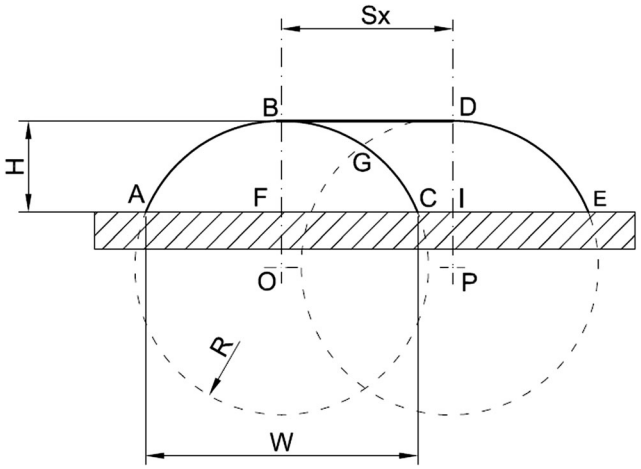

Fig. 1 Mathematical model parameters

The former is due to the higher oxidation kinetics and unmelted powders, and the latter depends on both the stability of powder flow and the interaction between the metallic powder, delivery gas and laser power [11, 12]. Both circular and elongated pores raise the stress intensity factor [13]. Yan et al. examined the influence of pore shape on fatigue fracture. In particular, they found that high pore shape factor determined a high fatigue strength limit [14]. In order to reduce the porosity inside the track, good methods are powder drying treatment, increment of laser power and the use of fine powder [15]. Chan and Lee demonstrated that, when two phases with different hardness coexist in a component, the interaction between the two structures causes a build-up of plastic strain in the softer phase and makes it more susceptible to crack initiation [16].

Variable cooling rate produces a non-uniform microstructure. As an effect, different structure, grain orientation, and lattice parameters after depositing AISI 4340 powders can be observed [17].

Zhang et al. studied the influence of thermal history on the microstructures and properties of a multilayer stainless steel 410 (SS410) thin wall [18].

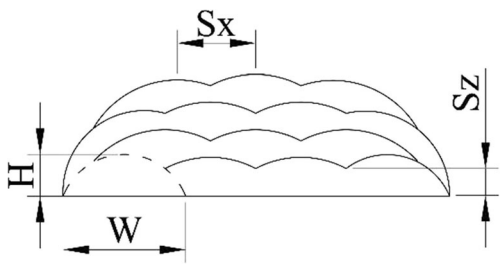

Fig. 2 Sketch of the cross section of a multilayer specimen

Table 2 Taguchi experimental plan

Sample	P (W)	v (mm/min)	Q (g/min)	E_d (J/mm^2)
1	1600	200	6	240
2	1600	300	8	160
3	1600	400	10	120
4	1750	200	8	263
5	1750	300	10	175
6	1750	400	6	131
7	1900	200	10	285
8	1900	300	6	190
9	1900	400	8	143

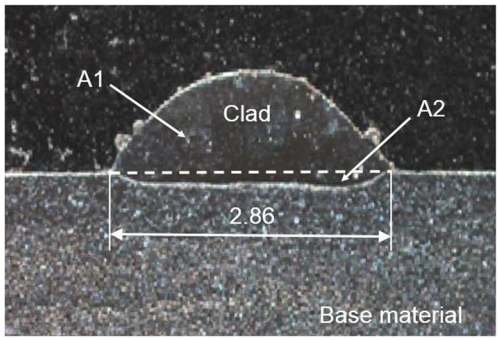

Fig. 3 Cross-sectional morphology of sample 3 produced by single-track deposition

Direct manufacturing and repairing of DLPD parts present high difficulties, and they are still a challenging process for industry, mainly for the selection of the optimum conditions and strategies. Marage steels are used in a wide variety of applications, including missile cases, aircraft forgings, structural parts, bearings, transmission shafts, dies, etc. These steels are used in aircraft and aerospace application, in which the superior mechanical properties and weldability of marage steels are the most important characteristics. As a tool steel, marage has excellent mechanical properties and stability during the age hardening process [19].

In the literature, just a few papers can be found on the multilayer deposition of marage steels by laser cladding technology that perform a systematic and comprehensive analysis of marage steel powder laser deposition process. Same papers are dedicated to the cladding of 18 Ni marage 300 steel parts [20–26].

Moreover, there are few studies that provide numerical or analytical method for the optimisation of the porosity and for the reduction of the defects typically resulting from the overlapping of layers. In fact, Shamsaei et al., in their overview on direct laser deposition, stated that research for increasing the quality of DLD parts primarily relies on a trial-and-error procedure to determine optimal process parameters. Furthermore, optimal process parameters are typically determined via extensive experiments, which usually require high experimental costs and a significant time investment. Since many interacting process parameters are involved, it is challenging to develop a comprehensive and general methodology for the optimisation of the direct laser deposition process [27].

In this paper, the effects of the main process parameters, i.e. laser power, scanning speed, powder flow rate, overlapping and step height, on the physical and metallurgical properties of 18 Ni (300) marage steel DLPD parts were investigated by analytical and experimental methods.

The mathematical model, which was available from Colaço et al., Zhang et al. and Angelastro et al., was implemented in order to obtain an optimal degree of overlapping between layers and between tracks [28–30]. The interface between the deposited marage 300 and the AISI 304 steel substrate was analysed by SEM. By means of

Table 3 W, H and D of single track

Sample	W (mm)	H (mm)	D (%)
1	2.97	1.01	11.0
2	3.11	0.93	12.4
3	2.86	0.80	10.1
4	3.35	1.29	11.2
5	3.18	1.01	11.5
6	2.66	0.51	28.2
7	3.40	1.53	10.7
8	2.89	0.65	23.5
9	2.87	0.66	17.6

Table 4 Process parameters used during the multilayer manufacturing

Sample	P (W)	v (mm/min)	Q (g/min)	Sx (mm)	O (%)	Sz (mm)
1	1600	200	6	2.15	27.52	0.59
2	1600	300	8	2.22	28.77	0.54
3	1600	400	10	2.02	29.30	0.46
4	1750	200	8	2.48	25.92	0.77
5	1750	300	10	2.29	28.19	0.59
6	1750	400	6	1.83	31.36	0.29
7	1900	200	10	2.61	23.47	0.94
8	1900	300	6	2.01	30.68	0.37
9	1900	400	8	2.00	30.57	0.38

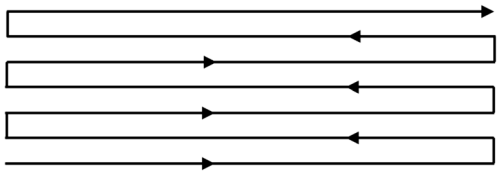

Fig. 4 Deposition strategy for each layer

a Taguchi experimental plan, the properties of the manufactured samples were analysed for what it concerned the density, dilution, microstructure, adhesion to substrate and microhardness. High-density samples, with a satisfactory level of porosity, were fabricated by the method proposed and tested in this work for successful additive and part repair applications.

2 Experimental condition and procedure

2.1 Experimental setup and materials

The investigated powder had a chemical composition equivalent to that of the 18 Ni (300) marage steel. The composition was determined by energy-dispersive X-ray (EDX) analysis (Table 1).

Marage steels comprise a special class of high-strength steels that differ from conventional steels in that they are hardened by a metallurgical reaction that does not involve carbon. Instead, these steels were strengthened by the precipitation of intermetallic compounds at temperatures of about 480 °C. The term marage derives from martensite age hardening and denotes the age hardening of a low-carbon, iron-nickel lath martensite matrix. One of the main virtues of marage steels is their excellent weldability. Perhaps, the characteristic that most enhances the weldability of marage steels is that their low carbon content produces a soft, ductile martensite on cooling. The powder size ranged from 5 to 40 μm. The true density of the material was 8.01 g/cm^3.

The substrate material was made of AISI 304 steel.

A 3-kW CO_2 laser and a powder supply system consisting of a pneumatic conveyor were used for the experiment. The mix of the powder and the partition of the flow into three equal flows of carrier gas and powder were achieved by a splitter and a coaxial nozzle that directed the powder flows into the fused metal pool.

Helium with a flow rate of 5 slpm was used as carrier gas, while argon with a flow rate of 11 slpm was used as shielding gas. The spot diameter was equal to 2 mm, and the substrate was made of an 8-mm-thick plate.

In order to obtain optimised degree of overlapping between adjacent layers and between tracks, a mathematical model was implemented.

2.2 Mathematical model

The mathematical model was used for calculating optimal values of hatch spacing between adjacent tracks (*Sx*) and between layers (*Sz*) of the deposited material (Fig. 1). The model was based on two fundamental hypotheses.

1. The deposition process was stationary: the quantity of powder at each deposited track was identical; the cross-sectional area of each track was uniform [29].
2. The transverse section of the deposited track was geometrically assimilated to an arc of circumference of height 꾈 and width with some degree of approximation [28–30].

Moreover, for known values of *W* and *H*, it is possible to calculate the value for the hatch spacing between adjacent

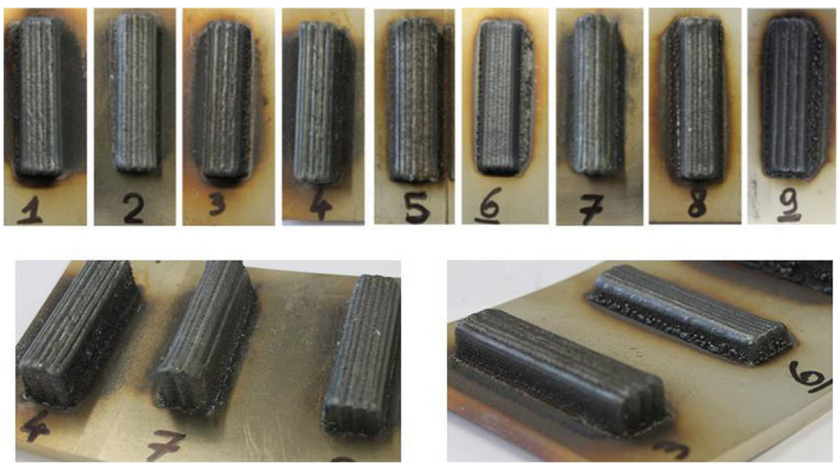

Fig. 5 Images of multilayer samples

Table 5 Final dimensions of multilayer samples

Sample	Real average dimension (mm)		
	Width	Length	Height
1	16.44	61.93	14.54
2	17.53	61.83	13.56
3	17.22	62.11	12.58
4	17.10	62.02	17.94
5	16.73	63.42	13.56
6	15.83	61.12	8.07
7	16.82	62.23	18.87
8	15.24	62.62	9.26
9	17.41	61.54	8.71

tracks (*Sx*), along the X-direction, which ensures a certain geometric regularity of the final surface of each deposited layer. Finally, it is possible to calculate the value of the hatch spacing between adjacent layers of material (*Sz*), along the Z-direction. This value has to guarantee an $O_{\%}$ that maximises the relative density of deposited tracks, a good adhesion between layers and hardness comparable with that of the original material.

After the abovementioned hypothesis, it is possible to introduce the following equation:

$$A_{ABC} = A_{BDEC} = A_{BDIF} = H{\cdot}Sx \tag{1}$$

where A_{ABC}, A_{BDEC} and A_{BDIF} are the areas of specific regions, as illustrated in Fig. 1.

In addition, it is possible to calculate the cross-sectional area (mm^2) with Eq. 2.

$$A_{ABC} = \left(\frac{\left(\frac{W}{2}\right)^2 + H^2}{2{\cdot}H}\right)^2 {\cdot}\arcsin\left(\frac{2{\cdot}\left(\frac{W}{2}\right){\cdot}H}{\left(\frac{W}{2}\right)^2 + H^2}\right) - \left(\frac{W}{2}\right){\cdot}\frac{\left(\frac{W}{2}\right)^2 - H^2}{2{\cdot}H} \tag{2}$$

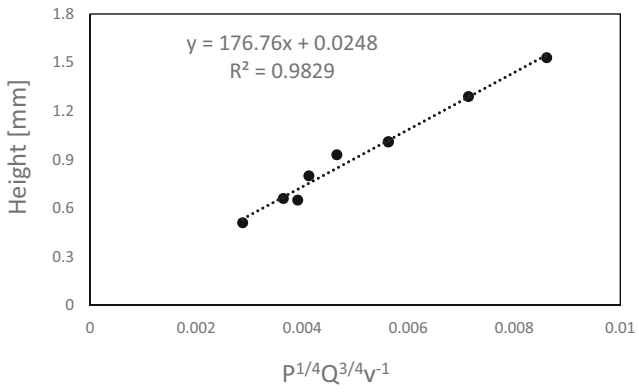

Fig. 6 Height as a function of $P^{1/4}Q^{3/4}v^{-1}$

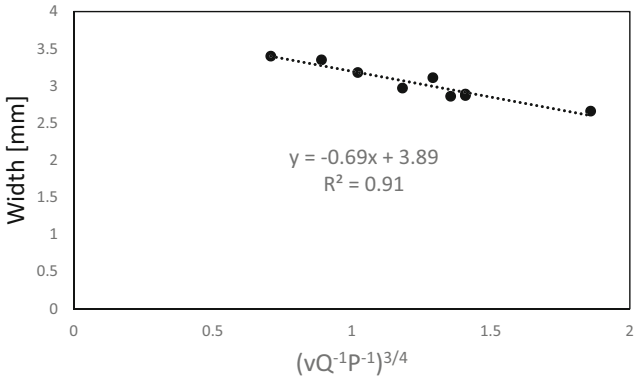

Fig. 7 Width as a function of $(vQ^{-1}P^{-1})^{3/4}$

Finally, it is possible to obtain optimal values of *Sx* (mm) and of $O_{\%}$ with Eqs. 3 and 4.

$$Sx = \frac{A_{ABC}}{H} = \frac{1}{H}\left(\frac{\left(\frac{W}{2}\right)^2 + H^2}{2{\cdot}H}\right)^2 {\cdot}\arcsin\left(\frac{2{\cdot}\left(\frac{W}{2}\right){\cdot}H}{\left(\frac{W}{2}\right)^2 + H^2}\right) - \left(\frac{W}{2}\right){\cdot}\frac{\left(\frac{W}{2}\right)^2 - H^2}{2{\cdot}H^2} \tag{3}$$

$$O_{\%} = \frac{W - Sx}{W} \cdot 100 \tag{4}$$

In these equations, *H* (mm) is the maximum height reached by the single track, *W* (mm) is the value of the maximum width, A_{ABC} (mm^2) is the area of the cross section, and $O_{\%}$ represents the degree of overlap between two tracks.

In order to apply these equations, it was necessary to measure the width and the height of the preliminary track, which was determined based on the experimental plan.

The model suggested by Angelastro et al. was used [30]. As shown in Fig. 2, the centre of the laser spot of the first track in even layers was displaced of *Sx* / 2 with respect to the first one of odd layers, so the odd layers had one extra track with respect to

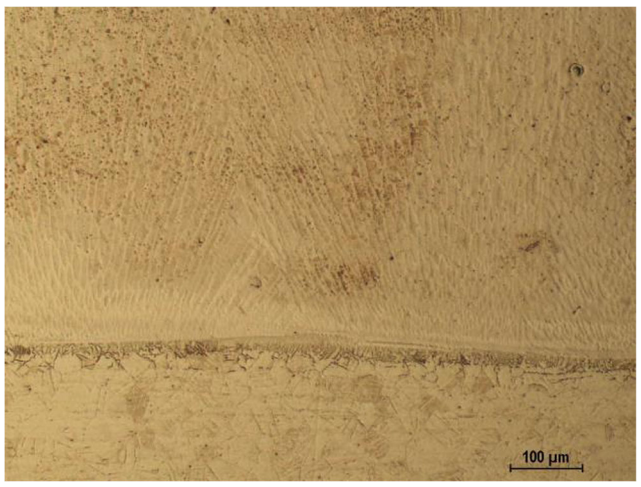

Fig. 8 Micrograph of marage (*upside*) and AISI 304 (*downside*) interface

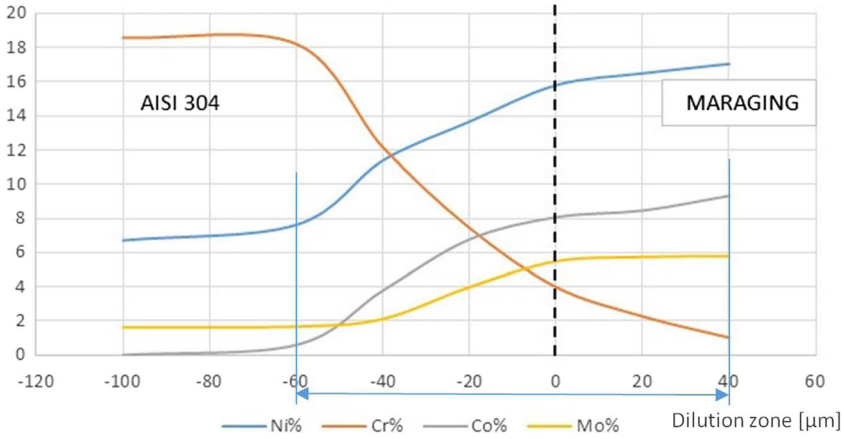

Fig. 9 Diagram of the most important chemical species in the transition zone (EDM analysis)

even ones. The laser was focused on the intersection of the two ideal circumferences, which is indicated with the letter G in Fig. 1.

After having calculated the circumference radius by Eq. 5, it is possible to determine optimal values of the laser step height, *Sz* (Eq. 6), for multilayer manufacturing.

$$R = \frac{1}{2 \cdot H}\left(\frac{W}{4} + H^2\right) \tag{5}$$

$$Sz = \sqrt{R^2 - \left(\frac{Sx}{2}\right)^2} - R + H \tag{6}$$

2.3 Single-track deposition

For the study of single track, the variations of three parameters were considered. They were laser power, scanning speed and powder flow rate. A Taguchi experimental plan was used to reduce the large number of trials required for a full factorial design. Based on the degrees of freedom of the experiments, an L9 orthogonal array was chosen to define the experimental schedule. Three factors were varied on three different levels, according to Table 2. The energy density was calculated as the ratio between the laser power and the product between scanning speed and the laser spot diameter, according to Eq. 7.

$$E_d = P/(v^*d) \tag{7}$$

Following the Taguchi plan reported in Table 2, preliminary single tracks were deposited in order to measure the width and the height of every clad (Table 3). Several macrosections of these tracks were made with the purpose to measure the geometrical features. Figure 3 shows a picture of sample 3, which highlights the cross-sectional morphology of the single track.

Dilution *D* was the ratio between the molten area in the base material (A2) and the molten area of the clad (A1 + A2) (see Fig. 3). Table 3 shows also the values for dilution for all parameter combinations. The calculation of *D* provides an estimation of the quality of the clad track in the process parameters.

2.4 Multilayer fabrication

Nine multilayer samples, each one consisting of 20 layers, were prepared by laser deposition of the marage steel powder on the AISI 304 steel substrates. The deposition area was a rectangle whose dimensions were 16 mm × 60 mm. The number of tracks for each layer depended on the *Sx* value. Geometrical measurements of the preliminary tracks were used to calculate *Sx* and *Sz* according to Eqs. 3 and 6. Table 4 contains these values together with other process parameters by which the multilayer samples were fabricated.

Figure 4 displays the deposition strategy for each layer. Figure 5 contains some pictures of the manufactured samples.

2.5 Characterisation of samples

The cross section of samples was cut, polished and etched for macrostructure and microstructure examinations. Nital 3 % etching was used to reveal macrostructure and microstructure in the deposited material. Glyceregia (15 mL

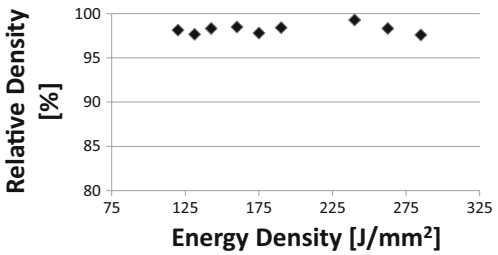

Fig. 10 Relative density as function of the energy density

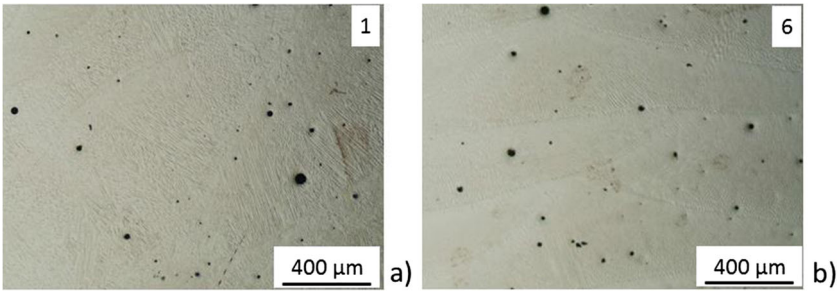

Fig. 11 Spherical porosity in sample 1 (**a**) and 6 (**b**) (see Table 2)

HCl, 10 mL glycerol, 5 mL HNO_3) etching solution was also used to reveal the interface with the substrate.

Optical and electron microscopes were used to analyse the specimen microstructure. Analysis of density and porosity was conducted on these blocks. The microhardness was measured for samples with the highest relative density.

The average dimensions of the multilayer were measured through a digital calliper (Table 5).

3 Results and discussion

3.1 Geometry of single track

Being capable to predict the laser track characteristics is important as a first step to fabricate a layer-by-layer object. The clad geometry (height and width) of each single track changes with the parameters (P, Q, v). Figures 6 and 7 show the mathematical relationship between those parameters and the height and width of the track. The height of the track, reported in Table 3, respected the proportionality with the function $P^{1/4}Q^{3/4}v^{-1}$, which was proposed by El Cheikh et al. (Fig. 6) [31]. A slight difference can be observed with El Cheikh et al., which can be attributed to the experimental error and to the different laser parameters used in both investigations. It is worthy to note that the powder flow rate is expressed in gram per second.

The R^2 coefficient between the width of the track and $(vQ^{-1}P^{-1})^{3/4}$ was equal to 0.91 (Fig. 7).

This model is able to predict the form and the geometrical characteristics of the single laser track cross sections from the principal laser parameters.

3.2 Adhesion and dilution

The analysis of the interface between the first deposited layer and the substrate shows a good adhesion for all samples (Fig. 8).

For laser cladding, it is often reported to keep dilution to a minimum to minimise the mixing between the clad layer and the substrate in order to maintain the properties of the baseline material. However, if dilution is zero, there is the risk of no fusion and bonding between cladding material and substrate. Therefore, a dilution between 2 and 10 % is generally accepted [32]. When clad layers do not mix, it is possible to maintain the initial properties of the deposited material [33]. That condition corresponds to a limited dilution. Otherwise, high dilution can allow stronger bonding between the clad and base material and may have beneficial effects in case of a component reparation [34]. Values of percentage dilution for all combinations of considered process parameters are reported in Table 3. Dilution ranges between 10 and 28 %.

The transition zone from substrate to clad can be described by its chemical composition. Figure 9 shows the concentration of the most important chemical species and the length of the transition zone for sample 3.

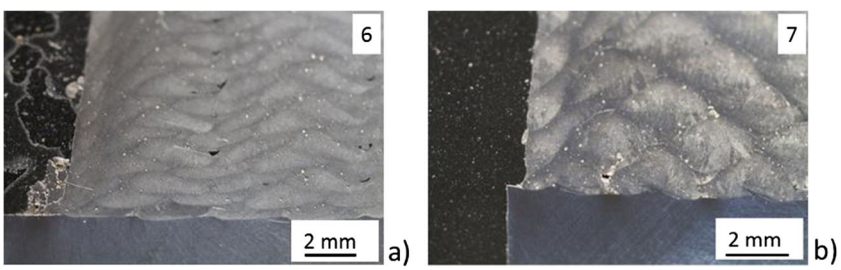

Fig. 12 Pores between layers for sample 6 (**a**) and 7 (**b**) (see Table 2)

3.3 Density and porosity

Density was measured by weighing the samples in air and subsequently in demineralised water, after coating them with a lacquer (Archimedes method). The coating prevented absorption of demineralised water by the specimen during the immersion. The sample density was calculated by Eq. 8.

$$\rho_s = \frac{m_s \rho_{H_2O}}{\left[m_s - m_{l+s}^{H_2O} + m_l\left(1 - \frac{\rho_{H_2O}}{\rho_l}\right)\right]} \quad (8)$$

where m_s is the mass of solid, m_l is the mass of lacquer, ρ_{H_2O} is the density of demineralised water, $m_{l+s}^{H_2O}$ is the mass of coated sample in demineralised water, and ρ_l is the density of the lacquer. The mass of the lacquer is determined as the difference between sample weights before and after coating.

The effect of energy density (E_d) on relative density (R_d) was plotted and analysed in Fig. 10.

Values of E_d ranged between 120 and 285 J/mm^2. This clearly indicates that R_d of built parts changed between 97.6 and 99.3 %. It is evident that the density was almost constant with the increase of energy density, reaching an average value of 98.2 %. This result confirms that the used mathematical model, together with the reduced experimental plan, allowed obtaining high values for the relative density with a low number of tests.

The analysis of porosity revealed different kinds of pores/voids, depending on the combination of process and design parameters.

First, almost circular shape geometry pores were detected. They are the result of the formation of gas bubbles that were trapped in the solidifying molten pool. Figure 11 displays the micrograph of porosity for samples 1 and 6 (see Table 2). Porosity formation was mainly due to material shrinkage and the balling effect [35].

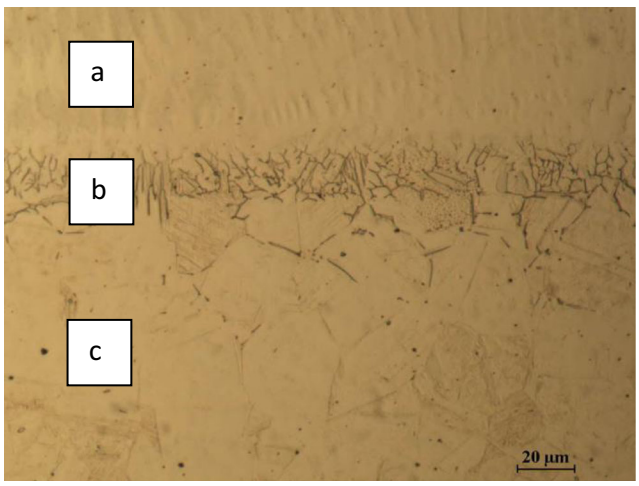

Fig. 13 Interface of the deposited material with the AISI 304 substrate

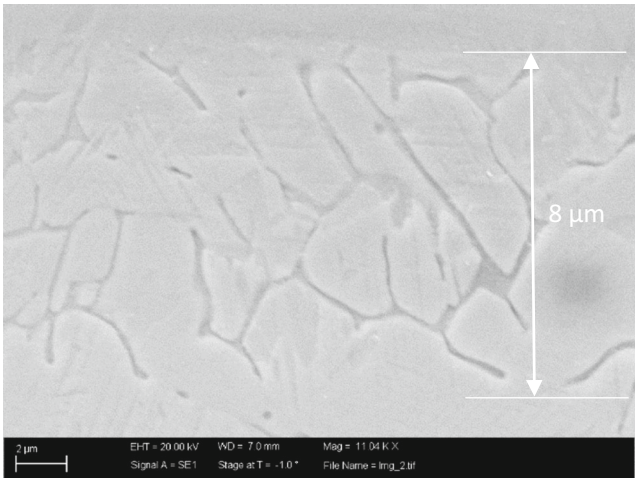

Fig. 14 Close-up of the refined grain with the border precipitate

Moreover, pores and voids can form due to lack of fusion between layers. At top layers, the lack of fusion occurred due to insufficient laser power, while closer to the substrate, they formed due to a high heat transfer rate [36].

These pores appeared as interlayer pores, having irregular shapes. The coalescence was significantly more important at the interface between adjacent layers, which gave an elongated appearance of the pore clusters (Fig. 12). This kind of porosity was confined to the substrate-clad interface. The 'inter-run porosity' is usually caused by low aspect ratio [33] or lack of fusion at the clad toe. The clad toe angle was related to the formation of inter-run porosity (Fig. 12).

3.4 Analysis of microstructure

Figure 13 shows a micrograph of the interface of one single clad that was deposited onto the AISI 304 sub-

Table 6 EDX analysis of the grain and border grain of the AISI 304 refined zone

Element	Concentration (%)	
	Grain	Border
Si	0.82	0.76
Mo	0.59	0.59
Ti	0.14	0.22
Cr	17.90	21.03
Fe	71.58	70.30
Co	0.97	1.22
Ni	8.00	5.88

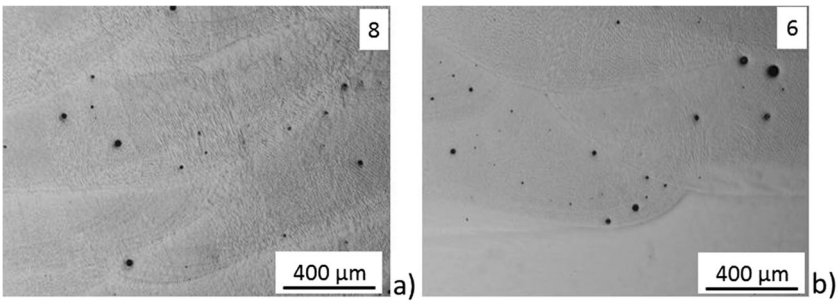

Fig. 15 Microstructure of sample 8 (**a**) and of sample 6 (**b**) obtained with a magnification ratio of ×50

strate. It is possible to distinguish among three zones. Zone "a," which corresponds to the marage solidified clad, shows a typical columnar/dendritic grain shape, which was due to re-solidification. Zone "b" presented an AISI 304 refined grain, which formed after local fusion, with border precipitates. Zone "c" was made of AISI 304 softly heat-affected zone whose grain size remained that of the base material and precipitates were absent.

Figure 14 shows a SEM close-up of AISI 304 refined zone with border grain precipitates. The thickness of the refined zone was 8 µm. Table 6 shows the EDX analysis of the grain and the border. The border was rich in chrome and cobalt, while nickel was a lower concentration.

In Fig. 15, the overlapping of the deposited tracks puts in evidence a quite regular layer, which confirms the hypothesis at the base of the mathematical model. Clad profile showed the important role assumed by the re-melting phenomenon, which occurred during the deposition of subsequent layers.

Microstructure was the result of a complex solidification process, which depended on the degree of constitutional supercooling. The combination of very fine martensitic structures of cellular and dendritic solidification formed the final microstructure. Solid-state transformation occurred locally where austenite grains rapidly cool and transform in Fe–Ni martensite with high dislocation density [37].

The grain size was refined. Micrographs in Fig. 16a–d reveal the contemporary presence of equiassic and elongated grains together with dendritic structures, as underlined by Amine et al. [38]. This morphology was similar to that obtained by Casalino et al. in the selective laser melting process of the same marage steel [39]. The different temperature gradients inside the track produced the characteristic morphology. In particular, according to the observation of Choi et al., the dendrites grew along a perpendicular direction with respect to the track boundary [40]. The growing direction of this structure points out the direction of the heat flux during the deposition process.

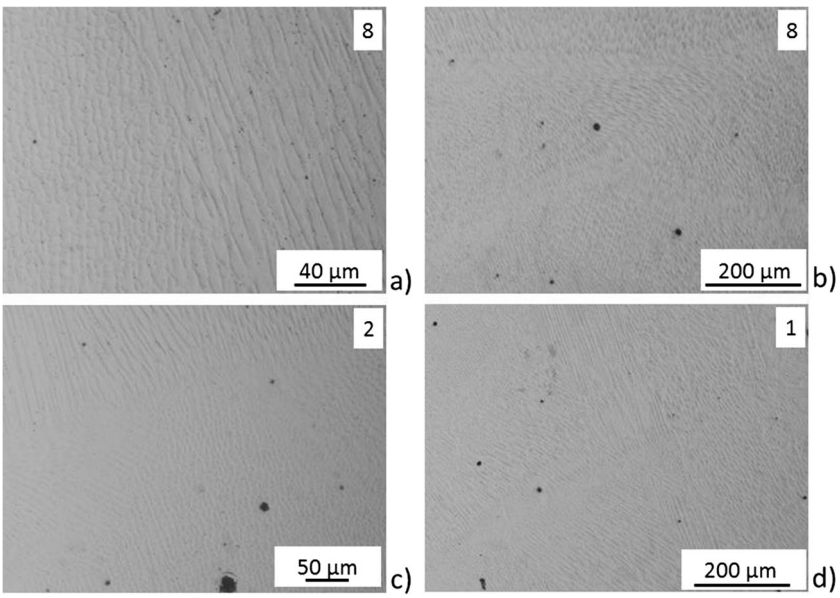

Fig. 16 Microstructure of sample 8, obtained with a magnification ratio of ×400 (**a**) and ×100 (**b**). Microstructure of samples 2 (**c**) and 1 (**d**) obtained with a magnification of ×200 and ×100, respectively

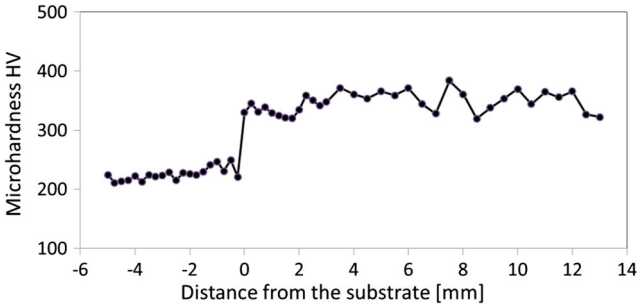

Fig. 17 Microhardness profile for sample 1

The dendrite growth across the track surface demonstrated a degree of re-melting of the deposited layer, which allowed a correct binding between the deposited layers and the feeded powder. This observation confirmed the fitness of the selected process parameters, at least for the early deposition layers.

No cracks were detected neither by the interface between each deposited layer or the substrate and the first layer.

Therefore, the structural integrity and martensitic transformation of this steel, which uses nickel as the primary strengthening element, account for a high mechanical strength with reduced ductility [41].

3.5 Microhardness

Microhardness of samples 1 and 2, which had the highest values of relative density, was measured, at various locations along the transversal section, using a Vickers indenter Remet HX 1000, with a 200-gf load for 15 s. Figures 17 and 18 show the microhardness profile along the cross section of the multilayer samples. Average microhardness of the deposited material was approximately 347–350 HV. These values of microhardness, obtained on as-deposited multilayer samples, are in line with typical microhardness of the 18 Ni (300) steel after solution annealing treatment, as reported in the ASM Handbook [19].

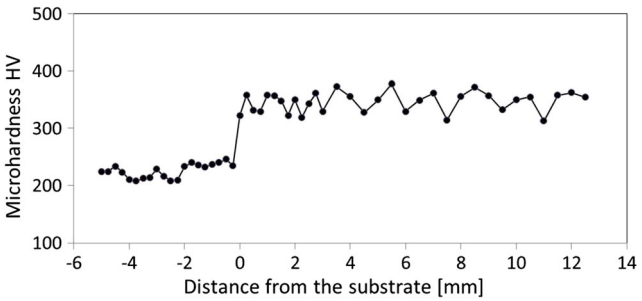

Fig. 18 Microhardness profile for sample 2

4 Conclusions

In this work, DLPD steel parts were manufactured using a CO_2 laser with a maximum power of 3 kW. In particular, 18 Ni (300) marage steel clads were deposited onto an AISI 304 substrate. A Taguchi plan was used to reduce the number of the experiments. The effects of laser power, travel speed and powder flow rate on the properties of built parts were studied. A mathematical model was used for the calculus of the optimal overlapping degree between adjacent layers and between successive tracks.

The following conclusions were drawn from the outcomes of the investigation.

- High-density parts can be produced with a limited effort using the process parameters selected by the statistical analysis and the mathematical model.
- Those parts are free of cracks and show a low number of pores and voids, which otherwise are numerous in multilayer laser powder deposition.
- The dilution with the substrate is as low as 10 to 28 %, which warrants the adhesion of marage to AISI 304 steel.
- The binding between the deposited layers and the feeded powder was good inasmuch the depositing tracks caused a superficial fusion of the previous layers, which was confirmed from the presence of elongated grains together with dendritic structures in the clad.

Acknowledgments The authors wish to remember that this research was founded by Project PON02_00576_3333604 INNOVHEAD "Innovative technologies for low emission, consume and operational cost of heavy duty engines" funded by the Italian National Operational Programme for Research and Competitiveness 2007–2013.

References

1. ASTM F2792-12a (2012) Standard terminology for additive manufacturing technology. ASTM International, West Conshohocken, Pennsylvania
2. Sears JW (1999) Direct laser powder deposition-state of the art, powder materials: current research and industrial practices. In: Marquis FDS, Editor. Proceedings of the 1999 Fall TMS Meeting, pp 213–226.
3. Toyserkani E, Khajepour A, Corbin SF (2005) Laser cladding. CRC Press, Boca Raton, Florida
4. Lu ZL, Li DC, Tong ZQ, Lu QP, Traore MM, Zhang AF, et al. (2011) Investigation into the direct laser forming process of steam turbine blade. Opt Lasers Eng 49:1101–1110
5. Peng L, Shengqin J, Xiaoyan Z, Qianwu H, Weihao X (2007) Direct laser fabrication of thin-walled metal parts under open-loop control. Int J Mach Tools Manuf 47:996–1002

6. Boisselier D, Sankaré S, Engel T (2014) Improvement of the laser direct metal deposition process in 5-axis configuration. Phys Procedia 56:239–249
7. Lewis GK, Schlienger E (2000) Practical considerations and capabilities for laser assisted direct metal deposition. Mater Des 21:417–423
8. Milewski JO, Lewis GK, Thoma DJ, Keel GI, Nemec RB, Reinert RA (1998) Directed light fabrication of a solid metal hemisphere using 5-axis powder deposition. J Mater Process Technol 75(1–3): 65–172
9. Bi G, Gasser A (2011) Restoration of nickel-base turbine blade knife-edges with controlled laser aided additive manufacturing. Phys Procedia 12:402–409
10. Wilson JM, Piya C, Shin YC, Zhao F, Ramani K (2014) Remanufacturing of turbine blades by laser direct deposition with its energy and environmental impact analysis. J Clean Prod 80: 170–178
11. Wang L, Pratt P, Felicelli SD, El Kadiri H, Berry JT, Wang PT et al (2009) Pore formation in laser-assisted powder deposition process. J Manuf Sci Eng Trans ASME 131.
12. Susan DF, Puskar JD, Brooks JA, Robino CV (2006) Quantitative characterization of porosity in stainless steel LENS powders and deposits. Mater Charact 57:36–43
13. Albaut GN, Grigor'ev-Golubev VV, Morozov NF, Proskura AV (1999) Influence of circular pores on the intensity of stresses. Mater Sci 35:76–81
14. Yan Y, Nash GL, Nash P (2013) Effect of density and pore morphology on fatigue properties of sintered Ti–6Al–4V. Int J Fatigue 55:81–91
15. Zhong C, Gasser A, Schopphoven T, Poprawe R (2015) Experimental study of porosity reduction in high deposition-rate laser material deposition. Opt Laser Technol 75:87–92
16. Chan KS, Lee Y-D (2008) Effects of deformation-induced constraint on high-cycle fatigue in Ti alloys with a duplex microstructure. Metall Mater Trans A 39:1665–1675
17. Sun G, Bhattacharya S, Dinda GP, Dasgupta A, Mazumder J (2011) Microstructure evolution during laser-aided direct metal deposition of alloy tool steel. Scr Mater 64:454–457
18. Zhang Y, Yu G, He X, Ning W, Zheng C (2012) Numerical and experimental investigation of multilayer SS410 thin wall built by laser direct metal deposition. J Mater Process Technol 212:106–112
19. ASM Handbook, Volume 1 properties and selection: irons, steels and high performance alloys (1990) ASM International, The Materials Information Company, United States of America, 1303, 1225–1236.
20. Lewis SR, Lewis R, Fletcher DI (2015) Assessment of laser cladding as an option for repairing/enhancing rails. Wear 330-331:581–591
21. Bergant Z, Grum J (2014) Heat treatment effects of laser cladded 12 Ni marage tool steel with Ni-Co-Mo alloys. J Heat Treat Mater 69(2):114–123
22. Bergant Z, Grum J (2014) The influence of chemical composition on residual stresses in NiCoMo alloy deposits on 12 Ni marage steel. Mater Sci Forum 768-769:449–455
23. Bergant Z, Grum J (2013) Influence of laser deposition technique on surface integrity of 12 Ni marage tool steel. Int J Microstruct Mater Prop 8(1–2):17–26
24. Zoran B, Marko SJ, Luis OJ, Janez G (2011) Laser cladding and heat treatment of Ni-Co-Mo marage steel. J ASTM Int 8(5).
25. Clare A, Olusola O, Folkes J, Farayibi P (2011) Laser cladding for railway repair and preventative maintenance. In: ICALEO 2011—Proceedings of 30th International Congress on Applications of Lasers and Electro-Optics: Laser Institute of America, pp 240–249.
26. Schwam D, Denney P, Kottman M (2014) Rejuvenation of steel dies with hot wire laser cladding. Trans N Amer Manufac 42(January):202–210
27. Shamsaei N, Yadollahi A, Bian L, Thompson SM (2015) An overview of direct laser deposition for additive manufacturing; part II: mechanical behavior, process parameter optimization and control. Addit Manuf 8:12–35
28. Colaço R, Costa L, Guerra R, Vilar R (1996) A simple correlation between the geometry of laser cladding tracks and the process parameters. In: Mazumder J, Conde O, Vilar R, Steen W (eds) Laser processing: surface treatment and film deposition. Kluwer Academic Publishers, Berlin, pp. 421–429
29. Zhang K, Liu W, Shang X (2007) Research on the processing experiments of laser metal deposition shaping. Opt Laser Technol 39: 549–557
30. Angelastro A, Campanelli SL, Casalino G, Ludovico AD (2013) Optimization of Ni-based WC/Co/Cr composite coatings produced by multilayer laser cladding. Adv Mater Sci Eng
31. El Cheikh H, Courant B, Branchu S, Hascoët J-Y, Guillén R (2012) Analysis and prediction of single laser tracks geometrical characteristics in coaxial laser cladding process. Opt Lasers Eng 50:413–422
32. Hofman JT, De Lange DF, Pathiraj B, Meijer J (2011) FEM modeling and experimental verification for dilution control in laser cladding. J Mater Process Technol 211:187–196
33. Steen WM (2010) Laser material processing, 4th edn. Springer Verlag, London
34. Schneider MF (1998) Laser cladding with powder: effect of some machining parameters on clad properties, University of Twente, Ph.D Thesis. Enschede, The Netherlands: Print Partners Ipskamp
35. Simchi A (2006) Direct laser sintering of metal powders: mechanism, kinetics and microstructural features. Mater Sci Eng A 428: 148–158
36. Yadollahi A, Shamsaei N, Thompson SM, Seely DW (2015) Effects of process time interval and heat treatment on the mechanical and microstructural properties of direct laser deposited 316L stainless steel. Mat Sci Eng A-Struct 644:171–183
37. Cabeza M, Castro G, Merino P, Pena G, Román M (2012) Laser surface melting: a suitable technique to repair damaged surfaces made in 14 Ni (200 grade) marage steel. Surf Coat Technol 212: 159–168
38. Amine T, Newkirk JW, Liou F (2014) Investigation of effect of process parameters on multilayer builds by direct metal deposition. Appl Therm Eng 73:498–509
39. Casalino G, Campanelli SL, Contuzzi N, Ludovico AD (2015) Experimental investigation and statistical optimisation of the selective laser melting process of a marage steel. Opt Laser Technol 65: 151–158
40. Choi J, Chang Y (2005) Characteristics of laser aided direct metal/material deposition process for tool steel. Int J Mach Tools Manuf 45:597–607
41. M.V.L. Ramesh, P. Srinivasa Rao, V. Venkateswara Rao. Structure–properties evaluation of dissimilar laser beam welds: marage steel and high strength low alloy steel. Journal of Material Science and Mechanical Engineering (JMSME), 2, 8; April–June, 2015, 42–45.